UC Santa Barbara
UC Santa Barbara Previously Published Works

Title

On delamination toughening of a 14YWT nanostructured ferritic alloy

Permalink

Authors

Alam, ME
Pal, S
Maloy, SA
et al.

Publication Date

DOI

Peer reviewed

On Delamination Toughening of a 14YWT Nanostructured Ferritic Alloy

M. E. Alama, S. Pala, S. A. Maloyb, G. R. Odettea*

a) Materials Department, University of California, Santa Barbara, CA 93106, USA

alam@engineering.ucsb.edu (M.E. Alam), soupitak@engineering.ucsb.edu (S. Pal)

b) Los Alamos National Laboratory, Los Alamos, NM 87545, USA

maloy@lanl.gov (S.A. Maloy)

*Corresponding author. Tel.: +1 (805) 893-3525; fax +1 (805) 893-8651

E-mail address: Odette@engineering.ucsb.edu (G.R. Odette)

Abstract

The FCRD NFA-1 is a high strength, irradiation tolerant nanostructured ferritic alloy (NFA) produced by ball milling argon atomized Fe-14Cr-3W-0.35Ti-0.25Y (wt.%) and FeO powders, followed by hot extrusion at 850ºC, and subsequent annealing and cross-rolling at 1000ºC. The microstructure of the resulting ≈ 10 mm thick NFA-1 plate is dominated by ultrafine sub-micron pancake shaped grains, and a large population of microcracks lying on planes parallel to the plate faces. Pre-cracked fracture toughness tests in four different orientations (L-T, T-L, L-S and T-S) show stable crack growth by ductile tearing, with peak load K_{Jc} from ≈ 88 to 154 MPa√m at ambient temperature. Stable crack tearing persists down to ≈ -175°C and is accompanied by extensive delamination due to the propagation of the microcracks. Depending on the specimen orientation, this unusual toughening mechanism is either due to reduction of crack tip stresses in thin ligaments formed by the delaminations (L-T and T-L), or 90° deflection of cracks initially running normal to the delaminations (L-S and T-S), thereby

suppressing cleavage in both cases. Understanding the fracture processes in NFA-1 is also important to its irradiation tolerance in nuclear service as well as its fabricability in making defect-free components such as thin-walled tubing.

Keywords: Nanostructured ferritic alloy; ODS ferritic steel, Texture; Delamination; Fracture toughness.

1. Introduction

The success of the Gen IV nuclear fission and future fusion reactors as a source of large-scale C-free power production depends on the development of new, high-performance structural materials that can safely support extended component lifetimes under the extremely hostile environment [1-2]. Nanostructured ferritic alloys (NFAs), which are a variant of oxide dispersion strengthened (ODS) steels, have high tensile, fatigue and creep strengths over a wide range of temperatures, excellent thermal stability up to more than 900ºC and unique irradiation tolerance, especially in managing high levels of helium [2-4]. These outstanding properties are directly, or indirectly, due to the presence of an ultrahigh number density of order $5 \times 10_{23}$ /m$_3$, ≈ 2.5 nm Y-Ti-O nano-oxides (NOs), submicron grains and high dislocation densities [2-5].

Recently a best-practice 14Cr-Y-W-Ti (14YWT) NFA was developed in a collaboration between Los Alamos National Laboratory (LANL), Oak Ridge National Laboratory (ORNL) and the University of California at Santa Barbara (UCSB). So-called FCRD NFA-1 was processed by first ball milling Fe-14Cr-0.25Y-3W-0.35Ti (wt.%) gas atomized powder with FeO powder to dissolve the Y and provide a proper balance of Ti and O [4, 6]. The mechanically alloyed powders were then canned, degassed, hot

extruded at 850₀C, annealed for 1 h and cross-rolled to an ≈ 50% thickness reduction, both at 1000₀C, to form an ≈ 10 mm thick plate.

While enjoying a host of outstanding properties, NFAs often have poor fracture toughness and high brittle-to-ductile transition temperatures (BDTT), as well as properties that are highly anisotropic [7-15]. NFA toughness is lower when the crack propagates parallel to the principal deformation (e.g., extrusion) direction, but is usually significantly higher in transverse orientations. In most cases, the limited literature on NFA fracture toughness has been reported only for the tougher transverse orientations. Thus, one objective of this study is to characterize NFA fracture toughness in all significant loading directions over a range of temperatures, from ambient (23°C) down to -196°C. In order to better understand the underlying mechanisms of fracture in NFA-1, the mesoscale microstructures and fracture surfaces were thoroughly characterized. The inexorable conclusion is that delamination mechanisms play a dominant role in the fracture behavior and toughness of NFAs, including NFA-1.

Delaminations/splitting are sometimes observed in Al-Li alloys [16-18] and structural steels [15, 19-31], leading to what is sometimes called delamination toughening. Although not always recognized, a common ingredient in the propensity for delamination in steels is deformation-processing leading to crystallographic texturing, and associated microstructures that are not isotropic. It is well established that delamination can help to lower BDTT, as we here and as some others argue [20-24, 27, 28], by reducing the triaxial stress concentration at the crack tip. Delaminations are mostly found at the mid-thickness region where the lateral stress is the highest. It has been reported that delamination in thermo-mechanically processed steels is generally due to deformation

incompatibilities between the two primary phases in duplex steels [19, 20, 27], and more generally, bands of aligned inclusions, and microstructural anisotropy [21, 22, 24-27, 29, 31], as well as texturing [15, 20- 26, 28, 29, 31] for other steels.

However, to our knowledge, there are no previous studies on the effect of pre-existing microcracks on delamination and fracture toughness. Further, almost all of the previous fracture studies involving delamination have been based on Charpy impact tests. Thus, a key objective of this research is to understand the causes and consequences of pre-existing microcracks to the fracture toughness of NFA-1 as a function of orientation and temperature, in specimens containing sharp primary pre-cracks in various pertinent loading orientations. Note, a very brief, in-progress summary of some results of this research were reported in a conference proceedings volume that covered several other topics, but with only a summary discussion [32].

Tensile tests in the longitudinal extrusion direction were also conducted at lower temperatures to evaluate the combination of strength-toughness of NFA-1, and to support both fracture testing and finite element analysis (FEM) simulations of the load-displacement curves of the pre-cracked bend bars (not discussed here). The tensile properties at higher temperature are reported elsewhere [33]. More quantitative finite element method (FEM) studies have been performed to understand the effects of delamination on development of near-crack tip stress fields is underway and will be reported in the future. Preliminary results can be found in [34].

We note that while the data and observations reported here on NFA-1 are at ambient temperature and below, they have significant implications to cold-working processes that are part of thermo-mechanical processing paths used to fabricate defect-free components,

like thin-walled tubing. Further, the as-fabricated deformation and fracture properties of NFA-1 are important to its subsequent behavior in service as, for example, by irradiation embrittlement. Finally, while we focus here on NFA-1, these results of this research have broad implications to NFAs in general, and in other structural metal systems that are subjected to delamination perhaps, in some cases, by intent.

2. Materials and Methods

2.1 Processing

NFAs are typically processed by ball milling Fe-Cr-Ti-Wand Y_2O_3 powders to mechanically alloy Y and O into solid solution [2,5,7-15,35]. However, in the case of NFA-1, Y was included in the melt prior to gas atomization and rapid solidification. The average size of the powder is ≈ 40 µm that ranging from ~25µm-100µm. Pre-alloying with Y was intended to explore the possibility of minimizing, or eliminating, the ball-milling step, as well as to produce more uniform distributions of NOs. The ball-milled powders were then sealed in a mild steel can, degassed at 400ºC, and hot extruded at 850ºC through a rectangular die. The extruded bar was annealed for 1 h, and then hot cross-rolled to an $\approx 50\%$ thickness reduction at 1000°C, to form an $\approx$15mm thick section including the can, containing an $\approx$10 mm plate. Further details of processing of NFA-1 can be found elsewhere [6, 33].

2.2 Microstructural characterization

Characterization of the NO and dislocation structures in NFA-1 are described elsewhere [6]. Figure 1a shows the orientations of the NFA-1 fracture specimens with respect to the extrusion, cross-rolling and thickness directions. Here we use the notation of L, T and S for the extrusion (L), transverse cross-rolling (T) and thickness (S) directions,

respectively. The corresponding plane section view direction are defined L, T and S: the extrusion section view is defined by the T and S (TS); the cross-rolling view section is defined by the L and S (LS), and the thickness view plate surface direction defined by L and T (LT). The corresponding three-dimensional (3D) mesostructure of the plate, composed of grains and microcracks, is shown in Figure 1b.

The surface sections were characterized by various combinations of: a) optical and scanning electron microscopy (SEM, FEIx30) equipped with energy dispersive spectroscopy (EDS); b) a dual beam Scanning Electron Microscope/Focused Ion Beam (SEM/FIB, FEI Helios 600); c) electron backscatter diffraction (EBSD, FEI Quanta 400F); and, d) transmission electron microscopy (FEI Titan and Technai TEMs) equipped with EDS and electron energy loss spectroscopy (EELS). Further details of the sample preparation and microstructural characterization technique can be found elsewhere [33].

The grains are pancake shaped due to the extrusion and cross-rolling deformations. When viewed perpendicular to the plate thickness (LT plate surface section view), the grains are roughly equiaxed, while in the extrusion and cross-rolling views (TS and LS planes) the grains are elongated in both cases. The longest (l) and shortest (s) dimensions of ~500 individual grains were analyzed using 'ImageJ64' software. The average grain size was taken as (l+s)/2 and the grain aspect ratio (GAR) as l/s.

SEM was used to image ≈ 250 (extrusion direction TS section views) and ≈ 500 (cross rolling direction LS section views) cracks, as illustrated by the low magnification images in Figs. 1b and c. These images were used to characterize the crack length, number, maximum opening width, separation distance, and number density per unit area on the sectioned surface. Note that in many cases adjacent cracks on the same plane were

separated by only small, intact bridging ligaments. In this case, they were counted as a single crack when the ligament size was ≤ 1 µm. EBSD (voltage: 20KeV, spot size: 4, step size: 0.05µm and working distance: 10mm) was used to characterize the texture induced by hot extrusion and cross-rolling for the different plate section views. TEM was used to investigate the micro-mechanisms of crack formation as described in detail elsewhere [36]. Optical microscopy provided macroscopic images of the fracture surfaces, and SEM was used for higher magnification fractography to detail delamination and the local fracture micro-mechanisms, both for the tensile and toughness tests. SEM was also used to characterize 150 to 270 of the coarser precipitate inclusions, since they act as nucleation sites for microvoids. The inclusions are most often arrayed in stringers along the extrusion direction. SEM and TEM were used to characterize the average size and spacing of the inclusions, as well as the stringer spacing. SEM and TEM with EDS and EELS were used to identify the compositions of the inclusions.

2.3 Tensile testing

The uniaxial tensile tests, loaded in the L-direction, were performed on flat dog-bone shaped, sub-sized (SSJ-2 type) specimens with a nominal gauge section dimensions of 5.0 mm length, 1.2 mm width and 0.5 mm thickness [33], a strain rate $\approx 10_{-3}$/s and over a range of temperatures from liquid nitrogen ($LN_2 \approx$ -196ºC) to 800°C. Additional details of the tensile tests are given in the SN-1 of supplemental information (SI), and elsewhere [33].

2.4 Fracture toughness

Fracture toughness tests were conducted from ambient down to LN_2 temperatures on fatigue pre-cracked single-edged notch three-point bend (3PB) specimens with nominal

7

dimensions of 16 mm in length, 3.3 mm width and 1.65 mm thickness, in four orientations as illustrated in Figure 1a (L-T, T-L, L-S and T-S, where the first letter designates the direction normal to the crack plane and the second letter designates the anticipated direction of crack propagation). A 810 MTS servo-hydraulic universal testing machine equipped with cooling chamber was used for this purpose. The specimens were fatigue pre-cracked under a low nominal cyclic load of 0 to 420 ± 50 N at 20 Hz to a nominal crack length-to-specimen width ratio (a/W) of ≈ 0.5. The fracture tests were generally conducted based on the ASTM E1921 standard practice [37], including constraint requirements. Of course, the E1921 procedure is not strictly valid for deflected cracks. However, a significant failure metric is the load and displacement at initiation that is reasonably reflected by K_{Jc}. The K_{Jc} was calculated at the maximum load, sometimes coincident with a small pop-in. Above -175°C crack initiation was followed by extensive stable crack growth by ductile tearing (except for one L-T specimen tested at -150ºC). Stable crack tearing is signaled by a decreasing load (P) in the P-displacement (Δ) curve. The crack initiation and final a/W were readily visible on the fracture surface after the specimen was broken in LN_2. The pre-crack a/W was measured as the average of 5 to 7 points along the crack front. Crack growth and resistance curves were not measured by a method such as unloading compliance. However, the a/W at a given P-Δ can be estimated by finite element simulations, e.g. the key curve method [38, 39]. A minimum of 2 tests was conducted in all cases and 3 for L-T at 23 and -150ºC and T-L at 23ºC. The number of tests was limited by the small quantity of available plate material. However, since the fracture process at and above -175°C is by ductile tearing, rather than cleavage, and since the corresponding K_{Jc} statistics are generally limited to small pop-in events (with the

exception at -150°C), the limited number of individual tests is not likely a serious issue in establishing the general fracture mechanisms and toughness trends in NFA-1.

3. Results and Discussion

3.1 Microstructural characterization

Figure 2a and b show a high magnification FIB/SEM, and EBSD 3D images of the NFA-1 plate, respectively. The grain statistics for the various section views are summarized in Table 1s in the supplemental information (SI) and elsewhere [33]. The pancake-shaped grains are elongated in the extrusion and cross-rolling directions. The longest grain dimension averages 866 nm in the extrusion direction, while the shortest in the corresponding thickness direction the average is ≈ 299 nm. The average grain size was taken as (l+s)/2 which was ≈ 580 nm for all section views. Of course, the sizes of the individual grains vary widely around these average values with an average standard deviation of ±480 nm. The GAR has an average of 1.5±0.4 in the LT plate surface section view and 2.7±1.45 in the LS and TS side section views. Most grains (≈ 80%) are < 1 µm, while fewer are in the range of 1-10 µm, and very few are more than 10 µm (see Fig. 1c). The extrusion and cross-rolling direction views of the TS and LS sections also reveal a large number of microcracks lying on planes normal to the plate thickness direction (parallel to the plate faces). The corresponding microcrack statistics are summarized in Table 1. The average opening at the crack center is ≈ 250 nm. The average distance between layers of cracks in the thickness direction is ≈ 16 µm. As shown in Fig. 1f, the crack lengths range from ≈ 2 to 105 µm. About 75% of cracks are below 15µm, and very few are over 50µm. The corresponding nominal observed averages are ≈12.5 µm. The

9

larger cracks are important since they serve as weak links that initiate cleavage fracture. The apparent microcrack number density per unit area averages $\approx 2.4 \times 10^9/m^2$.

The fine scale Y-Ti-O NO statistics ($d \approx 2.4$ nm, $N \approx 4.8 \times 10^{23}$ m^{-3} and $f \approx 0.6\%$) are reported elsewhere [6]. NFA-1 also contains coarser precipitates-inclusions as shown by the red arrows in Fig. 1c and summarized in Table 2s in the SI and Figure 1e. The inclusions are predominantly located at, or near, grain and prior powder boundaries, in the form of stringers aligned parallel to the extrusion and cross-rolling directions (Figs. 1c and 2a). The average inclusion size, spacing along the stringers and the stringer through-thickness spacing are ≈ 62, 270 and 2700 nm, respectively. EELS and EDS measurements identified the inclusions as Ti-rich (Ti-N-O: darker) oxynitrides with fewer Y-rich (Y-O: gray) oxides (see Fig. 1d). As shown by the histogram in Fig. 1e, the coarser inclusions ranged from ≈ 10 to 260 nm.

Figure 2b shows 3D EBSD maps of the grains and grain orientations. The misorientation angle ranges from $\approx 3°$ to 15° has been treated as low-angle subgrain boundary (indicated by red lines), and >15° as high-angle grain boundary (black lines) in EBSD IPF maps (Fig. 2b). The color-coding indicates the orientation distribution along the extrusion, cross-rolling and plate thickness compression directions. For the LT plate face view map, coded for poles in the z-direction, the grains are mostly red, indicating the dominance of (001) planes. As noted previously, the grains are nearly equiaxed in the LT plate face view (Fig. 2a). The corresponding LS view is mostly green, indicating the dominant {110}-fiber texture. Again as noted previously, the grains are elongated in the extrusion and cross-rolling directions and thinned (compressed) in the z-plate thickness direction. The texture index and GAR are only slightly higher in the extrusion direction, 4.83 and

2.71 ± 1.6, respectively, compared to the cross-rolling direction, 4.45 and 2.65 ± 1.3, respectively. TEM shows that low angle (~3º) sub-grain boundaries are formed inside the larger grains [36].

These observations clearly show that extrusion followed by cross-rolling creates {100}<110> plane-direction combinations, which are a brittle cleavage system in bcc Fe [24, 40-43]. Of course the α-fiber texture is very common in deformation-processed steels [15, 20-26, 28, 29, 31]. For example, Junceda *et al.* [29] and Kimura *et al.* [23] reported that the grains are oriented in <110> along the hot extrusion direction in 14YWT ODS steel, and in a tempered martensitic steel, respectively. Ukai *et al.* [15] also reported {100}<110> textured grains in parallel to rolling planes and rolling directions in a hot extruded, recrystallized and cold-rolled 15YWT ODS alloy leading to a lower cleavage BDTT in Charpy impact tests, due to delamination. Bourell [30] also found a similar texture component in warm-rolled low carbon steel.

Based on the elastic fracture stresses measured in tensile tests with loading in the short plate thickness direction, that will be reported elsewhere, the brittle {100}<110>-cleavage system in NFA-1 has an estimated low-temperature toughness of only ≈ 2 MPa√m, assuming a 100 µm diameter penny-shaped triggering microcrack. Notably, the microcrack cleavage system BDTT is much higher for NFA-1 than the corresponding BDTT for single crystal ferrite due to the much higher alloy strength relative to almost pure Fe [41-46]. As discussed elsewhere, and in future publications, the alloy strength-microcrack cleavage toughness relation has a significant effect on the shape of the master toughness temperature curve [45-46].

This paper focuses on characterizing the microcracks and their subsequent propagation as delaminations, which has a major corresponding effect on fracture properties. It is beyond the scope of this paper to address the microcracking mechanism, which we can only briefly summarize here. It was previously reported that the microcracks nucleated at the coarser precipitates, especially along prior powder grain boundaries [7, 13, 19]. However, this does not seem to be the dominant mechanism of microcrack formation in NFA-1, since the powders are much larger (average ≈ 40μm) than even the bigger grains (max≈ 13μm). Further, these grains are not preferentially associated with microcracks. As reported by Pal et al. [32, 35], the responsible deformation mechanism for microcracking can be summarized as follows. High temperature cross-rolling deformation results in a strong {100}<011> texture that also produces sessile a<001> dislocations on {100} planes by a/2[111] + a/2[1-1-1]→a[100] dislocation reactions. The resulting stack up of a[100] sessile dislocations forms a low angle sub-grain tilt boundary. Further deformation leads to pile up of additional a/2[111] slip dislocations at the {100} boundary, and creates a correspondingly high local stress-concentration. The leading dislocations form a cleavage crack opening nucleus on the {100} sub boundaries, as initially proposed by Cottrell [47]. The subsequent activation of the cleavage crack nuclei to form a population of microcracks is driven by deformation induced residual stresses as the plate cools to a temperature below the cleavage brittle to ductile transition temperature (BDTT).

Fig. 2c shows a bright field (BF)-TEM image of the crack propagation path, where the cross-sectional FIB lift-out is perpendicular to the crack front. Here, the hot extrusion direction is normal to the TEM lamella. The micrographs clearly show that the crack propagates within a single pre-existing grain in a transgranular manner. The selected area

diffraction pattern (SAD) from the locations marked 1 and 2 in Fig. 2c show that the foil normal is <110>. The microcrack front propagation direction is <110> along the primary deformation direction, which is normal to the TEM lamella in Fig. 2c. Similarly, weak beam dark filed imaging (WBDF) corresponding to the (002) spot in Fig. 2d, shows dislocation pile-ups around the crack and at the low angle subgrain boundary parallel to the crack. SAD patterns, shown in the insert in Fig. 2c, taken near the crack tip at the marked locations, show the general grain orientation is <110>. However, the pattern for location 2 is slightly misoriented (~3º) respect to that for location 1 in the same grain, even though they maintain the same general common near-<110> orientation. This indicates the presence of a low-angle subgrain boundary parallel to the crack propagation direction. Thus, these TEM observations fully support our hypothesis regarding this microcrack nucleation and propagation mechanisms. In general these observations are consistent with the more qualitative early findings of Tetelman and co-workers [48-50].

3.2 Tensile tests

The results of L-axis tensile test engineering stress-strain (s-e_p) curves as a function of temperature are shown in Fig. 3 and are summarized in Table 3s in the SI. Details of the high-temperature tensile test can be found elsewhere [33]. As expected the yield (s_y) and ultimate (s_u) stresses increase with decreasing temperature reaching a $s_y \approx 1555 \pm 121$ MPa and $s_u \approx 1643 \pm 112$ MPa at -196°C. Notably, the tensile total elongation strains (e_t) remain high down to -196°C. In all cases, the fracture surfaces are characterized by shallow ductile dimples (see Fig. 3b).

3.3 Fracture toughness at ambient temperature

The normalized ambient temperature ($\approx 23°C$) load-displacement (P-Δ) curves for the four different orientations (see Fig. 1a) are shown in Fig. 4a. This normalization involved adjusting the P-Δ data to a common a/W=0.5, so that the curves can be better intercompared. The L-S and T-S peak load (P_{max}, marked by a circle) are roughly similar and somewhat higher than those for the L-T and T-L orientations, which are also in themselves similar. The corresponding maximum load average K_{Jc} are $\approx$ 88 and 97 MPa$\sqrt{m}$ for L-T and T-L, respectively; and $\approx$ 154 and 140 MPa$\sqrt{m}$ for the L-S and T-S orientations, respectively. The P-Δ curves show a series of small pop-ins and an otherwise quasi-continuous load drop with increasing Δ following P_{max}. The P-Δ curve is associated with stable crack growth, and strong resistance curve behavior. Note, we did not construct resistance curve per se, in part due to the complications introduced by the delaminations.

In this case of ductile tearing beyond general yield, the P-Δ curves can be viewed as measures of cracked body strength and ductility, like in a tensile test. Note that the ductile tearing failure process is extremely graceful. The larger K_{Jc} for the T-S and L-S orientations is due to a higher P_{max} and Δ_{pmax} for deflected cracks. The K_{Jc} vary somewhat from specimen-to-specimen as shown by the scatter bars.

Post-test side-section images of the specimens in Fig. 4b, show that the cracks run in plane for L-T and T-L tests, but deflect by $\approx 90°$, to form Mode II cracks in both the L-S and T-S orientations. In the latter case, the deflected cracks run down delaminations parallel to the plate faces. The L-S and T-S P-Δ curves show a series of larger pop-ins, reflecting a larger distance between delamination microcrack initiation and arrest.

14

Representative fracture surfaces for the L-T and L-S (similar to T-L and T-S, respectively) orientations are shown in Fig. 5. Fig. 5a shows the different crack zones: notch 1; fatigue-pre-crack 2; stable crack growth 3; and post-test LN_2 cleavage fracture 4. The low magnification image (Fig. 5a) of the stable crack zone 3 shows the out-of-plane delaminations that develop along with tearing. The delaminations in the L-T and T-L (not shown) orientation are very similar. A higher magnification image in Fig. 5b reveals that the ductile tearing fracture surfaces are dominated by shear lips, or knife-edge ruptures, between minor out-of-plane delamination cracks. Ductile dimples are also observed. The microvoids likely initiate at the Ti-N-O and Y-O rich inclusions (Fig. 1d). No significant brittle cleavage is observed.

The maximum load K_{Jc} is controlled by the combination of the alloy strength and the crack tip opening displacement ductility. The strength relation derives from the fact that the ductile tearing occurs beyond general yielding of the pre-cracked 3PB specimens. The maximum load often occurs at small pop-ins, but this is not always observed. The initiation of crack tearing at maximum load is clearly seen on the ductile fracture surface and occurs at relatively low Δ_{pmax}, thus the K_{Jc} is modest. If the alloy was stronger, P_{max} would increase, while if it was more locally ductile Δ_p would increase. In both cases, this would lead to larger K_{Jc}. However, from a practical point of view, due to compliance effects, stable crack tearing beyond general yield is probably not a significant failure path in most engineering structures relevant to the application of NFA, and again this would lead to graceful failure.

Representative fracture surfaces for the L-S/T-S orientations are shown in Fig. 5c-e. Fig. 5c shows the P-Δ curve of L-S specimen and corresponding side-section *in-situ* optical

images at points 1 to 6 that show the 90º deflection from an in-plane Mode I to an out-of-plane Mode II crack. The load increases up to point-4. The micrograph corresponding to point-4 shows multiple crack-tip plastic zones (dark circles indicated by red arrows) due to the delamination. Note, these dark regions are due to out-of-plane lateral contraction dimples in the plastic zones. Numerous striation marks/delaminations normal to the loading direction (and parallel to the deviated crack front directions) are seen near the crack-tip (images 4-6 of Fig. 5c and Fig. 5d). The delaminations reflect the favourable orientation for microcrack propagation on the {100} cleavage planes along the pancake-shaped grains deformation <110> direction (Fig. 1). A relatively large pop-in occurs between points 4 and 5, along with a large increase in crack opening, marked by a green arrow in the micrograph for point-5. The micrograph for point-7 is a post-test low-magnification optical image of the fracture surface.

The combination of multiple delaminations and deflected cracks increases the remote loading K_{Jc}. Figure 5e shows a low magnification SEM image of the fractured T-S section that includes notch (1), pre-crack (2), and out-of-plane crack propagation (3) zones. Unlike L-T/T-L orientations (zone-3 of 5a), the L-S/T-S orientations shows virtually no, or very minimal, in-plane cracking near the initiation point (zone-3 of Fig. 5e). Additional T-S/L-S orientation 3PB tests have not been carried out, since in-plane fatigue pre-cracking is nearly impossible. Note most toughness data in the literature on NFAs is for L-T and/or T-L orientations.

3.4 Fracture toughness at lower temperatures

The L-T and T-L K_{Jc} at ambient and lower temperatures tests are summarized in Table 2 and Fig. 6. Representative P-Δ curves and the macroscopic images of the fracture

surfaces are shown in Fig. 7. The L-T and T-L $K_{Jc}(T)$ are similar, hovering around 100 MPa$\sqrt{}$m down to -125°C. Stable ductile tearing is observed down to -150ºC with one exception; one of the three L-T tests at -150ºC experienced a large cleavage fracture pop-in load drop near general yielding, with a lower $K_{Jc} = 52$ MPa$\sqrt{}$m. Note this specimen has a sharp notch in its uneven pre-crack front that may have created a secondary stress concentration leading to the pop-in. The fracture transition region behavior at -175°C is discussed in more detail below.

P-Δ curves in Fig. 7a and b show stable ductile tearing in the L-T and T-L orientations that is attributed to the delaminations (Fig. 7c and d). Selected temperatures (23, -100, and -150ºC) and a $\Delta \approx 0.8\pm0.2$ mm have been chosen as the reference conditions to characterize delaminations. Deeper (by visual inspection) and larger (>500 µm) delamination splits starting at, or near, the original crack front are classified as being major, while smaller (100-500µm), more isolated delamination splits are defined as minor (see Fig. 7e). The number of major (n_m) and total (major plus minor, n_t) delaminations, and their average (and maximum) lengths, l_t and l_m, increase with decreasing temperature as shown in Figure 7f and Table 4s in the SI. Note that there is no direct or one-to-one correlation between delamination distribution (Fig. 7f) and pre-test microcrack distribution (Fig. 1f). There are many smaller (<100µ) dilaminations that observed that are not included in the distribution plot. Larger and fewer in number microcracks propagate first to form the primary delaminations. The smaller microcracks do not propagate large distances, especially after the triaxial lateral stresses are relaxed by the primary delaminations.

The reason for the enhanced low temperature toughening is that the "crack-divider" delaminations occur in both the L-T and T-L orientations down to low temperature because of the microcracks. Basically and simply, this happens because the delaminations result in thin ligaments, which have peak stresses that are below those needed for cleavage down to the low temperatures. In contrast to the triaxial, plane-strain crack tip stress state, absent delamination, the thin ligament sections transition to a more biaxial plane-stress state. As a result, the peak stresses ahead of the crack tip decrease by a factor of up to ≈ 3, falling below the critical local fracture conditions required to initiate cleavage [4, 24, 38]. In part this is due to there being more delaminations at lower temperatures, resulting in even thinner ligaments and lower peak stresses relative to the yield stress. It is not until the temperature below -150 to -175°C that the blunting crack tip stresses are sufficient to drive cleavage before the delaminations form. Further, explanations of these classical effects are given in the SN-2 of supplemental information.

Figure 8 shows representative SEM images of fracture surfaces for low-temperature toughness tests. Local fracture morphologies are almost identical in both orientations down to -150°C (see Fig. 1s in SI). Larger shallow, crater-like features surrounded by knife-edge shear lips are observed, as shown in Fig. 8a, with smaller ductile microvoid dimples (see insert) decorating their bottoms. In contrast, both the tests of the L-T and T-L orientations at -196°C are characterized by classical, quasi-cleavage facets (Figure 8b). Compared to higher temperature tests (see example in Fig. 7a), the load-displacement (P-Δ) curves for L-T tests at -175°C show only a small amount of plastic post yield displacement, Δ_{pmax}, prior to a large cleavage load drop. This more brittle behavior as reflected in the fracture surfaces in Fig. 8c, showing three zones. The ductile tearing in

zone 1 (similar to Fig. 8a) experiences limited delamination. Extensive cleavage faceting is observed in zone 3, similar to the higher magnification image in Fig. 8b, and is associated unstable crack propagation. The ductile dimples at the bottom of the crater-like features are observed in zone 2 (see Fig. 8d), mark the transition between the stable and unstable crack propagation. The corresponding L-T K_{Jc} at -175°C is 70 ± 2 MPa√m, falls between ductile tearing delamination dominated case, at higher temperature, and cleavage initiation at -196°C. In contrast, the T-L tests exhibit ductile tearing and stable crack growth at -175°C, and a somewhat higher $K_{Jc} = 86 \pm 3$ MPa√m (see Table 2 and Fig. 7b). The -175°C T-L test delaminations in the tougher orientation are similar to those at higher temperatures.

In summary, with one exception, fracture of NFA-1 down to -150°C is dominated by ductile tearing and stable crack growth, largely due to delaminations that either shield the crack by deflection or reduction of triaxial stresses. K_{Jc} decreases at lower temperature and fracture occurs entirely by cleavage at -196°C. Thus a reasonable estimate of the BDTT of NFA-1 is -175°C.

The delaminations derive from the propagation of a population of microcracks in the as-extruded and cross-rolled NFA-1 plate. Since the delaminations are similar down to -150°C, the L-T and T-L toughnesses are remarkably isotropic compared to many other NFAs, that typically have tougher transverse versus a much more brittle deformation direction orientations. For example, an as-extruded bar of MA957 was found to be extremely brittle in the axial direction, but much tougher in transverse orientation, where the cracks deflect by 90° [7], similar to the behavior in the L-S and T-S orientations of NFA-1.

The multiple underlying fracture mechanisms in the cross-rolled NFA-1 plate are not unique in this class of alloys. The cross rolled plate is an extreme case, with pre-existing microcracks, but even when they are not present brittle {100}<011> texturing leads to low toughness orientations in the primary deformation directions. The presence of brittle textures depends on the processing route. For example, while typical as-extruded high temperature deformation processing does not result in microcracks, this NFA condition still has extremely low toughness in the extrusion direction with a <110>-fiber texture. In contrast, we have found that shear-dominated hydrostatic extrusion does not produce brittle textures in either the radial or axial directions [32, 51]. Thus the results reported here are very important to developing processing routes for NFA to fabricate defect-free components.

In order to provide additional perspective, Figure 9a compares the $K_{Jc}(T)$ of NFA-1 to similar nanostructured alloys [8-13]. With one possible exception, NFA-1 has the lowest brittle to ductile transition temperature (BDTT) in both orientations. The dashed rectangle highlights two other 14YWT heats that have higher toughness than NFA-1 in their L-T orientation as is the case for a MA957 round bar in the L-R orientation, both due to crack deflection. However, the fracture properties of these alloys are highly anisotropic, as highlighted by the dashed oval, with very low toughness and higher BDTT (e.g., -84ºC for L-T vs 18ºC for T-L tests on the 14YWT heat SM10) [9]; and also for MA957 in the C-R and C-L orientations (equivalent to T-L in the plate). Note, most previous NFA fracture tests were carried out only in the tough orientation. A combination of fracture toughness as a function of yield strength for different structural alloy in Fig. 9b, show that NFA-1 exhibits a very good combination of strength and toughness values compared

20

to Ni- and Ti-based alloys and other steels (except some HSLA steels tested at higher temperatures) [52-56].

3.5 Delamination and toughening mechanisms

Delaminations increase toughness either by crack deflection or by a reduction in triaxial stresses as schematically illustrated in Figs. 10a and 10b. The underlying mechanism is propagation of a population of pre-existing microcracks that form during processing. The mechanism of microcrack formation was briefly summarized here, but a more detailed evaluation of the dislocation level mechanisms is described elsewhere [32, 36].

In general, the number and depth of primary (major) delaminations increases with decreasing temperature as illustrated in the low magnification fracture surfaces at 23ºC to -175ºC shown in Figs. 7c and d, and summarized in Table 4s. At 23°C the primary, and likely first, delamination is in the middle of the uncracked ligament, splitting the crack front in half at the location of the peak transverse stress. The transverse stress peak then moves to the middle of the two halves producing one additional major split. The delaminations are accompanied by a reduction in the internal crack tip stresses that cannot reach the critical stress-stressed volume condition required for cleavage [4, 24, 57]. Thus, fracture can only take place by ductile tearing and microvoid coalescence producing shallow dimples on the fracture surface [4]. The finite element method (FEM) was used to simulate the P-Δ curve with no crack extension for both plane strain and stress state conditions based on the EPRI estimation procedure [38]. The curves are for single-edged notch bend (SENB) specimen plus a yield stress of 1201 MPa, and a Ramberg-Osgood strain hardening exponent of N = 20, with α =1. Other parameters that are used in the EPRI estimation procedure can be found in supplemental figure (Fig. 2s).

Figure 10c compares the FEM curves to corresponding T-L test data at -150ºC. The measured P_{max} falls between the plane strain and plane stress. The actual measured P gradually falls off after P_{max}, due to crack tearing with increasing Δ_p. Clearly, NFA-1 manifests a large amount of effective engineering ductility even for fracture by tearing of an initially sharp pre-crack. A more quantitative finite element method study of the effects of delamination of three-dimensional crack tip fields that are informed by the observations reported here is underway and will be reported in the future. Preliminary results can be found in [34]. However further discussion is beyond the scope of this experimentally focussed paper.

The L-S and T-S tests experience crack deflection as illustrated in Figs. 4 and 5. The primary crack travels only a short x-distance before arresting at a delamination. Continued increments of Δ result in the propagation of the 90° deflected delaminations and splitting of the specimen. Such delamination cracks are common in some composites, but rarer in metals. The loading-crack mode mixing for such kinking delamination cracks has been extensively studied [58-59]. However, for this work we simply define a higher initiation T-S and L-S K_{Jc} at P_{max}.

4. Summary and Conclusions

The fracture toughness of 14YWT NFA-1 was characterized over a wide range of temperatures in all relevant loading orientations. The results and conclusions can be summarized as follows:

- The FCRD NFA-1 extruded, and cross-rolled plate contains a bimodal size distribution of predominantly sub µm pancake-shaped grains, along with a large

population of microcracks lying on planes parallel to plate faces. The microcracks are associated with the combination of a strong {001}<110> texture in the crack planes, which is a brittle cleavage system in bcc-Fe, and residual stresses that develop during the thermo-mechanical processing.

- The focus of this paper is on the consequences of pre-existing microcracks. However, the underlying microcracking mechanism is also understood. As detailed elsewhere [32, 36], the key micromechanism is texturing leading to the formation of a {001}<110> cleavage system and reactions between glissile a/2<111> dislocations to form sessile a<100> dislocation stack-ups that constitute a {100} subgrain boundary. The microcracks nucleate at dislocation pile-ups at the subgrain boundary and the leading dislocations form a nanocrack opening displacement, following the theory of Cottrell [47]. Both local pile-ups and residual stresses then drive formation of µm-scale cracks at temperatures below the Fe-Cr ferrite {001}<110> cleavage system BDTT.

- Ambient temperature toughness tests show ductile tearing with a peak load K_{Jc} from ≈ 88 to 154 MPa√m.

- Extensive stable ductile tearing is observed both at L-T and T-L orientations from room temperature down to -150ºC, and in the T-L orientation down to -175°C, marking an effective BDTT.

- Ductile tearing occurs down to such low temperatures due to extensive delaminations that form by the propagation of the pre-existing microcracks.

- Delaminations in the L-T and T-L orientations split the crack front into thinner sections, leading to a reduction in both stress triaxiality and local tip stresses, thereby suppressing cleavage, consistent with FEM modeling reported separately.

- Delaminations in the L-S and T-S orientations result in 90° crack deflection and higher effective toughness mixed-mode fracture.

- The low-temperature toughness measured in this FCRD-NFA-1 alloy is much improved and more isotropic compared to most previous studied NFA.

References

[1]	S.J. Zinkle, G.S. Was, Materials challenges in nuclear energy, Acta Materialia 61 (2013) 735-758.

[2]	G.R. Odette, M.J. Alinger, B.D. Wirth, Recent developments in irradiation-resistant steels, The Annual Review of Materials Research, 38 (2008) 471-503.
[3]	Y. Dai, G.R. Odette, T. Yamamoto, The effects of helium in irradiated structural alloys, R. Konings (Ed.): Comprehensive nuclear materials", 1_{st} Edition, Atlanta, GA: Elsevier, 2012.
[4]	G. R. Odette, Recent progress in developing and qualifying nanostructured ferritic alloys for advanced fission and fusion applications, JOM, 66 (2014) 2427-2441.
[5]	S. Ukai, Oxide dispersion strengthened steels, R. Konings (Ed.): Comprehensive nuclear materials, 1_{st} Edition, Atlanta, GA: Elsevier (2012) 241-271.
[6]	N.J. Cunningham, Y. Wu, G.R. Odette, D.T. Hoelzer, S.A. Maloy, Characterization of a larger best practice heat of 14YWT in annealed powder, HIP consolidated and extruded forms, DOE/ER-0313/54 (2013), DOE Fusion Reactor Materials Program Semiannual Progress Report (2013).
[7]	M.J. Alinger, G.R. Odette, G.E. Lucas, Tensile and fracture toughness properties of MA957: implications to the development of nanocomposited ferritic alloys, Journal of Nuclear Materials, 307-311 (2002) 484-489.
[8]	D.A. McClintock, D.T. Hoelzer, M.A. Sokolov, R. K. Nanstad, Mechanical properties of neutron irradiated nanostructured ferritic alloy 14YWT, Journal of Nuclear Materials, 386-388 (2009) 307-311.
[9]	D.T. Hoelzer, J. Bentley, M.K. Miller, M.K. Sokolov, T.S. Byun, Development of high-strength ODS steels for nuclear energy applications, in: Proceedings of the ODS 2010 Materials Workshop, Qualcomm Conference Center, 17–18 November, 2010.
[10]	T.S. Byun, J.H. Kim, J.H. Yoon, D.T. Hoelzer, High temperature fracture characteristics of a nanostructured ferritic alloy (NFA), Journal of Nuclear Materials, 407 (2010) 78-82.
[11]	M.A. Sokolov, D.T. Hoelzer, R.E. Stoller, D.A. McClintock, Fracture toughness and tensile properties of nanostructured ferritic steel 12YWT, Journal of Nuclear Materials, 367-370 (2007) 213-216.
[12]	Ch.Ch. Eiselt, M. Klimenkov, R. Lindau, A. Möslang, G.R. Odette, T. Yamamoto, D. Gragg, Tensile and fracture toughness properties of the nanostructured oxide dispersion strengthened ferritic alloy 13Cr–1W–0.3Ti–$0.3Y_2O_3$, Journal of Nuclear Materials, 417(2011) 193-196.

[13]	P. Miao, G.R. Odette, T. Yamamoto, M. Alinger, D.T. Hoelzer, D. Gragg, Effects of consolidation temperature, strength and microstructure on fracture toughness of nanostructured ferritic alloys, Journal of Nuclear Materials, 367-370 (2007) 208-212.
[14]	R. Kasada, S.G. Lee, J. Isselin, J.H. Lee, T. Omura, A. Kimura, T. Okuda, M. Inoue, S. Ukai, S. Ohnuki, T. Fujisawa, F. Abe, Anisotropy in tensile and ductile–brittle transition behavior of ODS ferritic steels, Journal of Nuclear Materials 417 (2011) 180-184.
[15]	S. Ukai, W. Izawa, N. Oono, S. Hayashi, Y. Kohno, S. Ohtsuka and T. Kaito, Charpy impact property related to {100} cleavage fracture in 15Cr ODS steel, Materials Science and Technology, 30 (2014) 1709-1714.
[16]	K. T. V. Rao, W. Yu, R. O. Ritchie, Cryogenic toughness of commercial aluminum-lithium alloys: Role of Delamination Toughness, Metallurgical Transactions A, 20A (1989) 485-497.
[17]	K. T. V. Rao, R. O. Ritchie, Mechanical properties of AI-Li alloys – Part 1: fracture toughness and microstructure, Materials Science and Technology, 5 (1989) 882-895.
[18]	S. Kalyanam, A. J. Beaudoin, R. H, Dodds Jr., and F. Barlat, Delamination cracking in advanced aluminum–lithium alloys- Experimental and computational studies, Engineering Fracture Mechanics, 76 (2009) 2174-2191.
[19]	J. Pilhagen, R. Sandstrom, Loss of constraint during fracture toughness testing of duplex stainless steels, Engineering Fracture Mechanics, 99 (2013) 239-250.
[20]	M.S. Joo, D-W. Suh, J.H. Bae, H.K.D.H. Bhadeshia, Role of delamination and crystallography on anisotropy of Charpy toughness in API-X80 steel, Materials Science and Engineering A, 546 (2012) 314-322.
[21]	X. Min, Y. Kimura, T. Kimura, K. Tsuzaki, Delamination toughening assisted by phosphorus in medium-carbon low-alloy steels with ultrafine elongated grain structures, Materials Science & Engineering A 649 (2016) 135–145.
[22]	Y. Kimura, T. Inoue, Influence of carbon content on toughening in ultrafine elongated grain structure steels, ISIJ International 55 (2015) 1135–1144.
[23]	Y. Kimura, T. Inoue, F. Yin, K. Tsuzaki, Delamination toughening of ultrafine grain structure steels processed through tempforming at elevated temperature, ISIJ International, 50 (2010) 152-161.
[24]	T. Inoue, F. Yin, Y. Kimura, K. Tsuzaki, S. Ichiani, Delamination effect on impact properties of ultrafine grained low carbon steel processed by warm caliber rolling, Metallurgical and Materials Transactions A, 41A (2010) 341-355.

[25]	J. Chao, C. Capdevila, Anisotropy in mechanical properties and fracture behavior of an oxide dispersion Fe20Cr5Al alloy, Metallurgican and Materials Transactions A, 45A (2014) 3767-3780.
[26]	A.L. Rouffie, P. Wident, F. Delabrouille, B. Tanguy, J. Crepin, A. Pineau, V. Garat, B. Fournier, Influences of process parameters and microstructure on the fracture mechanisms of ODS steels, Journal of Nuclear Materials 433 (2013) 108–115.
[27]	X. L. Yang, Y-B. Xu, X-D. Tan, D. Wu, Influences of crystallography and delamination on anisotropy of Charpy impact toughness in API X100 pipeline steel, Materials Science & Engineering A 607 (2014) 53–62.
[28]	Y. Kimura, T. Inoue, F. Yin, K. Tsuzaki, "Inverse temperature dependence of toughness in an ultrafine grain-structure steel, Science, 320 (2008) 1057-1060.
[29]	A.G. Junceda, M.H. Mayoral, M. Serrano, Influence of the microstructure on the tensile and impact properties of a 14Cr ODS steel bar, Materials Science and Engineering A, 556 (2012) 696-703.
[30]	D.L. Bourell, Texture induced cleavage delamination of warm-rolled low carbon steel, Metallurgical Transaction A, 14A (1983) 2487-2496.
[31]	B.L. Bramfitt, A.R. Marder, A study of the delamination behavior of a very low carbon steel, Metallurgical Transactions A, 8A (1977) 1263-1273.
[32]	S. Pal, M. E. Alam, G. R. Odette, S. A. Maloy, D. T. Hoelzer, J. Lewandowski, "Microstructure, Texture and Mechanical Properties of the 14YWT Nanostructured Ferritic Alloy NFA-1", Mechanical and Creep Behavior of Advanced Materials Ch 4, I. Charit et al. (Eds) Springer (2017) 43-54.
[33]	M.E. Alam, S. Pal, K. Fields, S.A. Maloy, D.T. Hoelzer, G.R. Odette, Tensile deformation and fracture properties of a 14YWT nanostructured ferritic alloy, Materials Science and Engineering A, 675 (2016) 437-448.
[34]	C. Ruggieri, M.E. Alam, G. R. Odette, A numerical investigation of delamination effects on the fracture behavior of a 14YWT nanostructured ferritic alloys (NFA-1)", DOE/ER-0313/61 (2016), DOE Fusion Reactor Materials Program Semiannual Progress Report, 61 (2016) 19-29.
[35]	M.J. Alinger, G.R. Odette, D.T. Hoelzer, On the role of alloy composition and processing parameters in nanocluster formation and dispersion strengthening in nanostructured ferritic alloys, Acta Materialia, 57 (2009) 392-406.
[36]	S. Pal, M. E. Alam, G. R. Odette, D. Hoelzer, S. Maloy, Microstructure, texturing, microcracking and delamination behavior of NFA-1, DOE/ER-0313/58

	(2015), DOE Fusion Reactor Materials Program Semiannual Progress Report, 58 (2015) 66-82.
[37]	ASTM E1921-13a, Standard Test Method for Determination of Reference Temperature, T_o, for Ferritic Steels in the Transition Range, ASTM International, West Conshohocken, PA, 2013.
[38]	T.L. Anderson, Fracture Mechanics: Fundamentals and Applications", 3rd Ed, Taylor & Francis Group, FL, USA, 2005.
[39]	H. Ernst, P.C. Paris, M. Rossow, J.W. Hutchinson, Analysis of load-displacement relationship to determine J-R curve and tearing instability material properties, Fracture Mechanics, ASTM STP 677, C. W. Smith, (Ed.), American Society for Testing and Materials, (1979) 581-599.
[40]	W. R. Tyson, R.A. Ayres, D.F. Stien, Anisotropy of cleavage in bcc transition metals, Acta Metallurgica, 21 (1973) 621-627.
[41]	M.L. Hribernik, Cleavage oriented iron single crystal fracture toughness, PhD Thesis, University of California Santa Barbara, CA, USA (2006).
[42]	M.L. Hribernik, G.R. Odette, M.Y. He, On the initiation and arrest cleavage fracture toughness of ferrite, DOE /ER-0313/40 (2006), DOE Fusion Reactor Materials Program Semiannual Progress Report, 40 (2006) 74-79.
[43]	Y. Qiao, A.S. Argon, Brittle-to-ductile fracture transition in Fe–3wt.%Si single crystals by thermal crack arrest, Mechanics of Materials 35 (2003) 903–912.
[44]	G.T. Hahn, The influence of microstructure on brittle fracture toughness, Metallurgical Transactions A, 15A (1984) 947-959.
[45]	G.R. Odette, T. Yamamoto, H.J. Rathbun, M.Y. He, M.L. Hribernik, J.W. Rensman, Cleavage fracture and irradiation embrittlement of fusion reactor alloys: mechanisms, multiscale models, toughness measurements and implications to structural integrity assessment, Journal of Nuclear Materials, 323 (2003) 313-340.
[46]	G.R. Odette, H.J. Rathbun, M. Hribernik, T. Yamamoto, M. He, P. Spätig, A multiscale approach to measuring and modeling cleavage fracture toughness in structural steels, V. Getta et. al. (Eds): Materials Issues for Generation IV Systems (2008) 203-226.
[47]	A.H. Cottrell, Theory of brittle fracture in steel and similar metals, Transactions of the metallurgical society of AIME, 212 (1958) 192-203.

[48]	A.S. Tetelman, W.D. Robertson, Direct observation and analysis of crack propagation in iron-3% silicon single crystals, Acta Metallurgica, 11 (1963) 415-426.
[49]	A.S. Tetelman, The effect of plastic strain and temperature on microcrack propagation in Fe-3Si, Acta Metallurgica, 12 (1964) 993-1004.
[50]	L.E. Kaechelets, A.S. Tetelman, Statistical investigation of microcrack formation, Acta Metallurgica, 17 (1969) 463-475.
[51]	S. Pal, M.E. Alam, G.R. Odette, J. Lewandowski, D.T. Hoelzer, S.A. Maloy, "Characterization of microstructure and texture of NFA-1 for two deformation-processing routes", Fusion Materials Semiannual Progress Report DOE/ER-0313/ 58, 2015, pp. 29–41.
[52]	T.V. Philip, T.I. McCaffrey, Ultrahigh strength steels, Mechanical Engineering, New York and Basel-Marcel Dekker, (1997) 149-162.
[53]	Y. Tomita, Effect of microstructure on plane-strain fracture toughness of AISI 4340 steel, Metallurgical Transaction A, 19A (1988) 2513-21.
[54]	R.O. Ritchie, B. Francis, W.L. Server, Evaluation of toughness in AISI 4340 alloy steel austenitized at low and high temperatures, Metallurgical Transactions A, 7A (1976) 831-838.
[55]	S. Maropoulos, N. Ridley, J. Kechagias, S. Karagiannis, Fracture toughness evaluation of a HSLA steel, Engineering Fracture Mechanics, 71(2004) 1695-1704.
[56]	18 Percent nickel maraging steels: Engineering properties. Ni Development Institute, Publication No. 4419, Inco Europe Limited, (1976) 29-58.
[57]	W.J. Yang, G.R. Odette, T. Yamamoto, P. Milao, M.J. Alinger, M. Hribernik, J.H. Lee, A critical stress–critical area statistical model of the $K_{Jc}(T)$ curve for MA957 in the cleavage transition, J. Nucl. Mater. 367-370, (2007) 616-620.
[58]	J.W. Hutchinson, Z. Suo, Mixed mode cracking in layered materials, Advances in Applied Mechanics, 29 (1991) 63-191.
[59]	K. Tohgo, H. Ishii, Elastic-plastic fracture toughness test under mixed mode I-II loading, Engineering Fracture Mechanics 41 (1992) 529-540.

List of Tables

Table 1. Crack statistics of NFA-1 at different plate views

Views	Crack opening width (nm)	Crack separation distance (µm)	Crack length (µm)	Crack density (m^{-2})
LT	-	-	-	-
LS	252 ± 142	16.3 ± 4.7	10.2 ± 8.9	3.45 x 10^9
TS	205 ± 130	15.2 ± 4.8	14.9 ± 12.6	1.34 x 10^9

Table 2. Low temperature fracture toughness (K_{Jc}) of NFA-1 at L-T and T-L orientations

Temp ($_o$C)	L-T (MPa$\sqrt{m}$)	T-L (MPa$\sqrt{m}$)
23	88 ± 12	97 ± 8
-50	113 ± 16	91 ± 13
-100	101 ± 4	96 ± 2
-125	102 ± 2	93 ± 5
-150	79 ± 23	92 ± 5
-175	70 ± 2	86 ± 3
-196	37 ± 4	44 ± 2

List of Figures

Fig. 7   (a and b) Representative NFA-1 L-T and T-L load displacement curves at various temperatures; (c and d) the corresponding macroscopic fracture surfaces showing the delaminations; (e) an SEM image showing how major versus minor delaminations and their lengths are defined; and, (f) the number (n_m) and length (l_m) of major delamination as a function of orientation and temperature.

Fig. 8   (a) SEM images of the fracture surfaces showing large shallow dimple-like features at -150ºC and a higher magnification insert showing microvoid dimples on the bottom of the larger features; (b) cleavage facets for the -196°C test, and (c) a L-T fracture surface at -175ºC, revealing delaminations (1), microvoid dimples and craters shown in Fig. d (2), and cleavage facets (3).

Fig. 9   Comparison of the NFA-1: (a) fracture toughness as a function of temperature with other ODS/NFAs [8-13, Hoelzer: personal communication], and (b) combined strength – K_{Jc} with different alloys [52-56].

Fig. 10   A schematic illustration of the: (a) transverse delamination mechanism (L-T and T-L); (b) crack deflection mechanism (L-S and T-S); and (c) FEM simulations of load-displacement (P-Δ) for plane strain and stress at -150ºC.

Fig. 1 (a) The specimen orientations and definition of the view; (b) pre-existing microcracks; (c) a representative higher magnification image of microcracks and inclusion stringers showing how crack spacing, opening and separation distance are defined; (d) EDS and EELS spectra showing the Ti-N-O rich precipitate inclusions (top), and SEM/EDS showing Y-O rich precipitates inclusions (bottom); (e) the size distribution of the coarser precipitate inclusions; and, (f) the distribution of microcrack lengths.
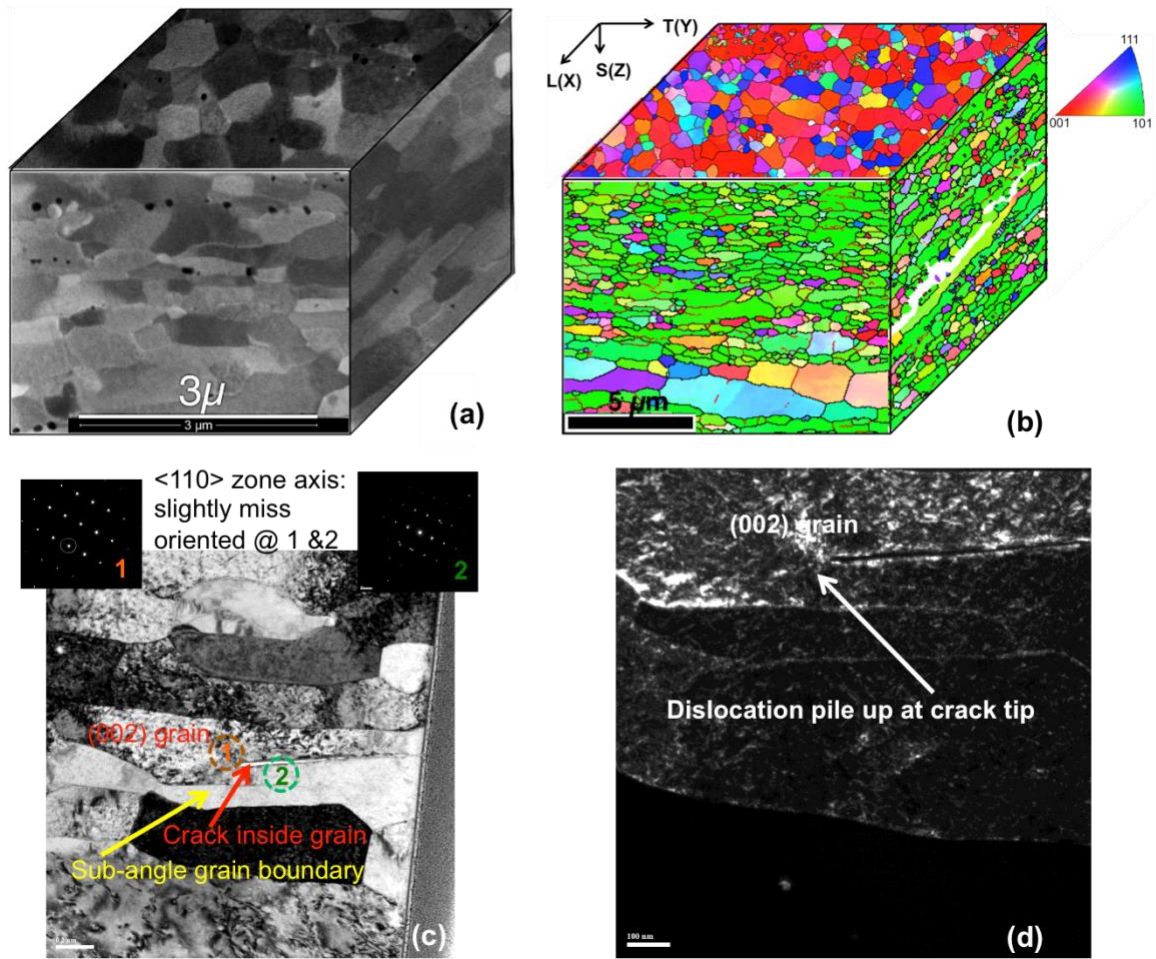
Fig. 2 3D images of NFA-1: (a) showing FIB/SEM grain structures; (b) EBSD inverse pole figure (IPF) maps showing strong <110> texture along the extrusion direction (ED) and (001) plane grains lying parallel to the L-T plate face; (c) a BF-TEM image of the crack propagation front at a subgrain boundary; and, (d) a weak beam dark field image corresponding to the (002) spot from inset SAD pattern 1 in (c). The crack is on a (002) plane and propagates in the <110> foil normal direction.
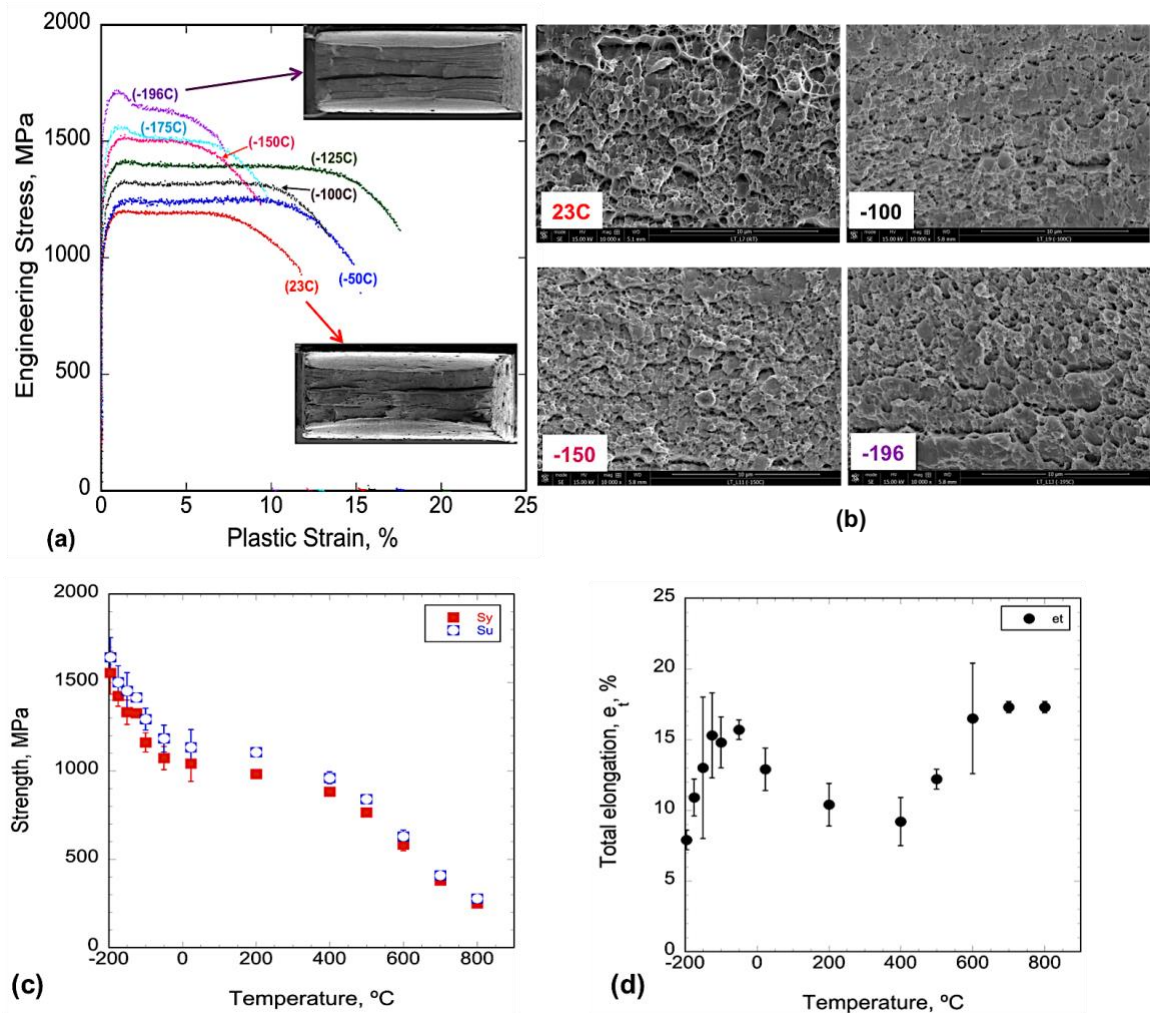
Fig. 3   (a) Engineering stress- plastic strain curves of L oriented tensile specimens tested at room to liquid nitrogen temperatures along with selective low magnification SEM images of the fracture surfaces; and (b) high magnification SEM images showing almost identical ductile fracture from room temperature down to -196ºC. Tensile strengths and ductility from 800ºC to LN_2 are also plotted in: (c) the 0.2% yield (s_y) and ultimate (s_u) stress; and (d) total elongation (e_t).
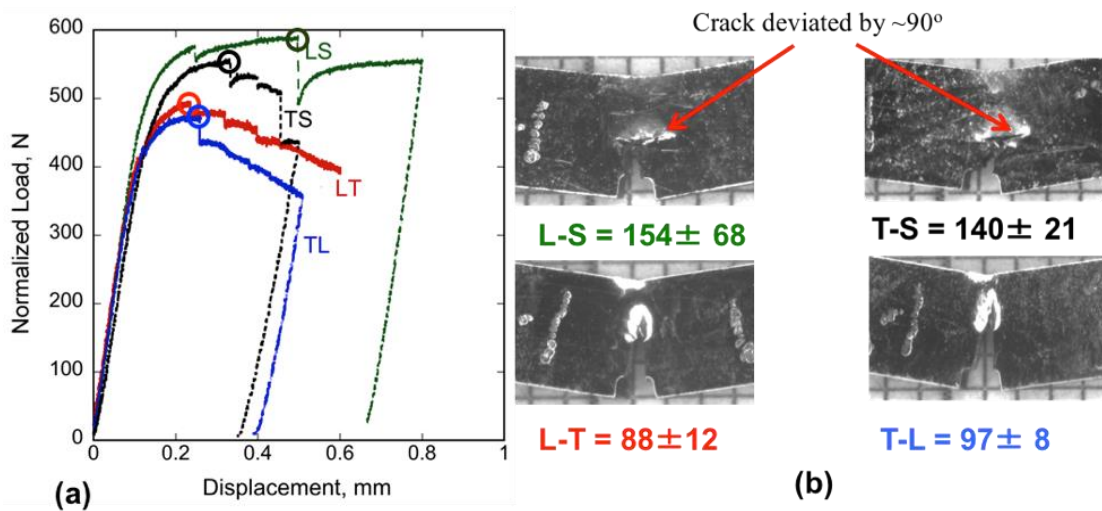
Fig. 4   Representative NFA-1: (a) load-displacement curves for 3PB tests at 23°C in the four orientations; and, (b) corresponding macroscopic side views of the propagated crack along with the corresponding K_{Jc} (MPa√m). Red, blue, green and black colors represent L-T, T-L, L-S, and T-S orientations, respectively.
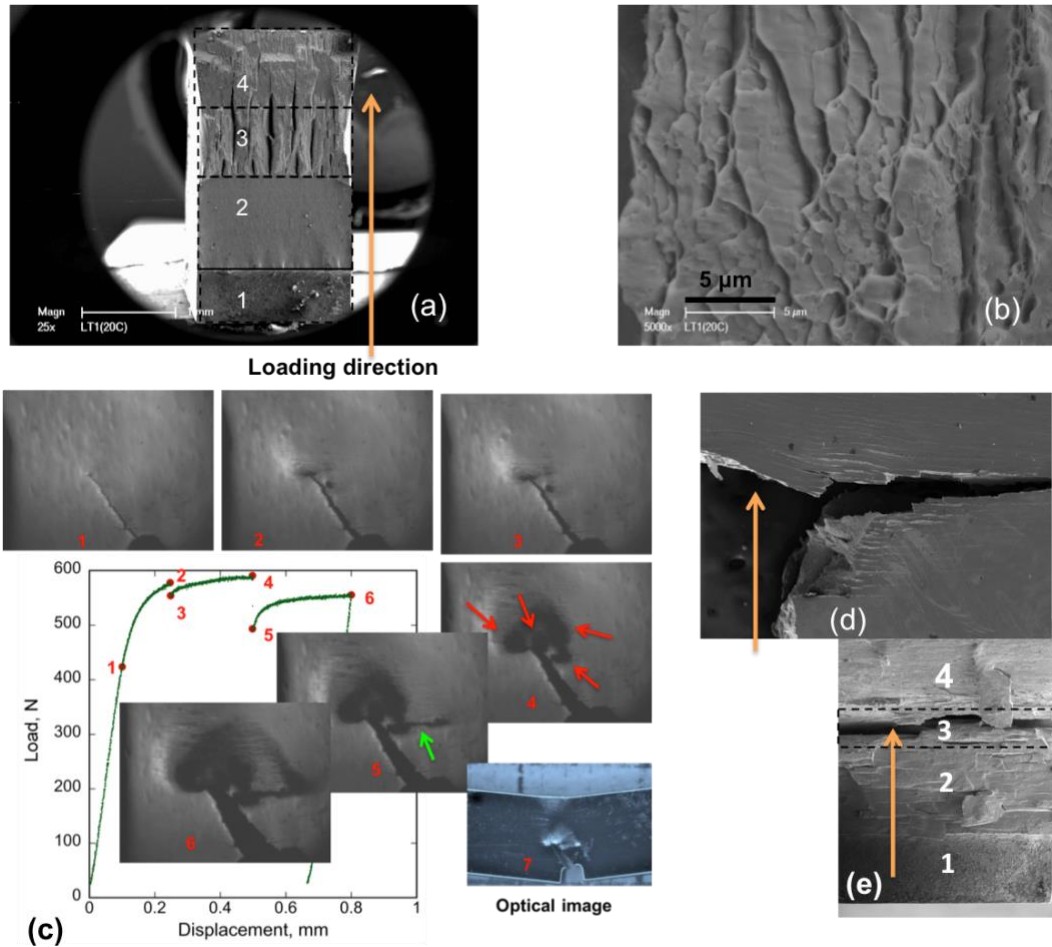
Fig. 5   Representative ambient temperature micrographs: (a) a SEM fracture surface image of the L-T orientation showing the different specimen zones: 1-notch; 2-pre-crack; 3–crack tearing; and 4-final fracture in liquid nitrogen; (b) a higher magnification image of zone-3; (c) a P-Δ curve and its corresponding *in-situ* images at points 1 to 6 for the L-S orientation. The red arrows at point-4 show multiple plastic zones and the green arrow at point-5 shows crack propagation. Point-7 is a post-test macroscopic view of the specimen; (d) SEM images showing the 90° crack deflection for the T-S and L-S orientations along with many micro-delaminations parallel to the deflected crack; and, (e) a macroscopic view of a fractured face that includes notch (1), pre-crack (2), and out-of-plane crack propagation (3) zones.
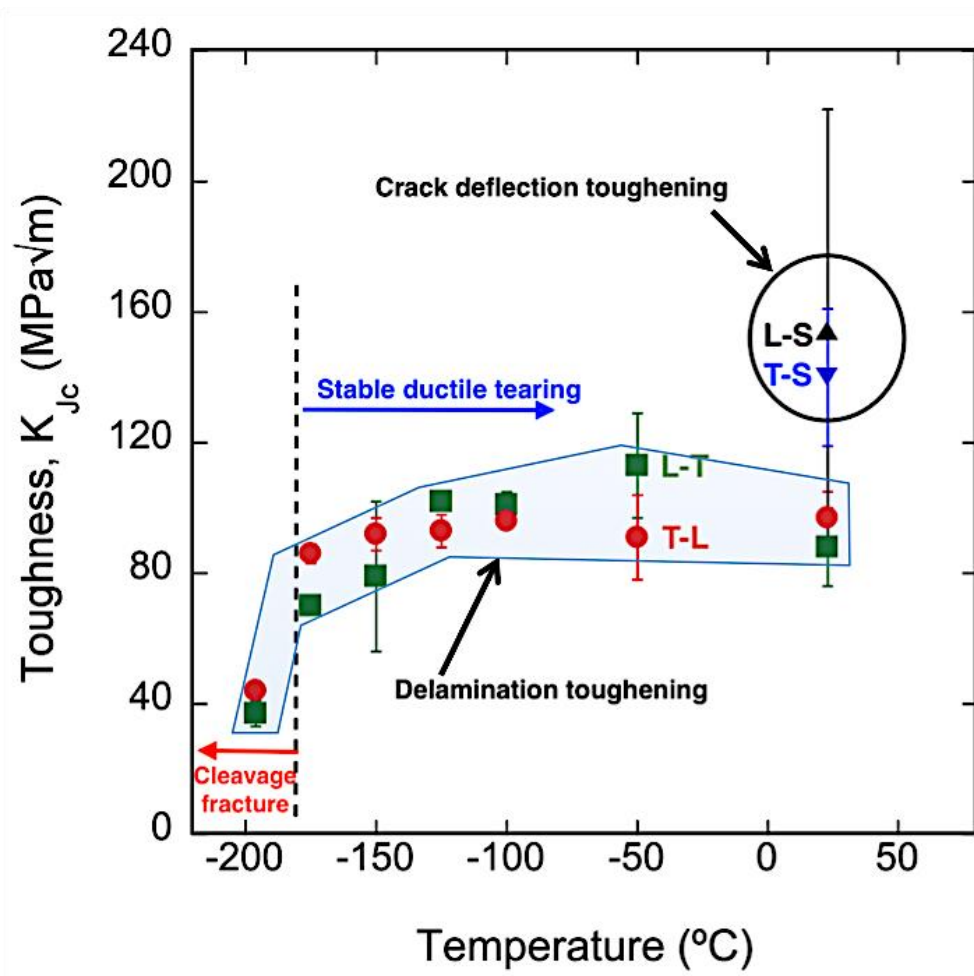
Fig. 6   The K_{Jc} (MPa√m) of NFA-1 as a function of temperature for the 4 orientations [32]. Green, red, black and blue colors represent L-T, T-L, L-S, and T-S specimens, respectively.
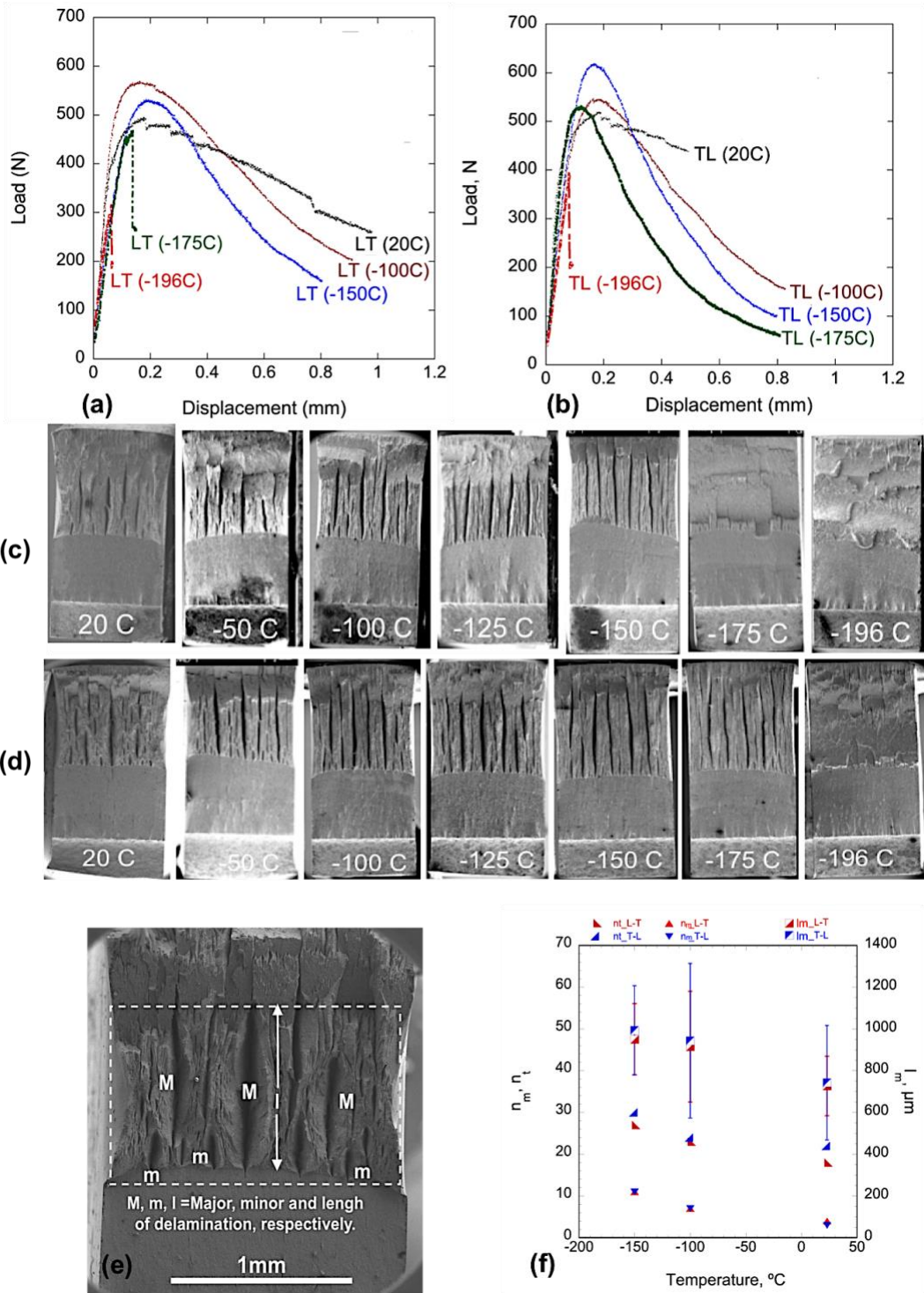
Fig. 7   (a and b) Representative NFA-1 L-T and T-L load displacement curves at various temperatures; (c and d) the corresponding macroscopic fracture surfaces showing the delaminations; (e) an SEM image showing how major versus minor delaminations and their lengths are defined; and, (f) the number (n_m) and length (l_m) of major delamination as a function of orientation and temperature.
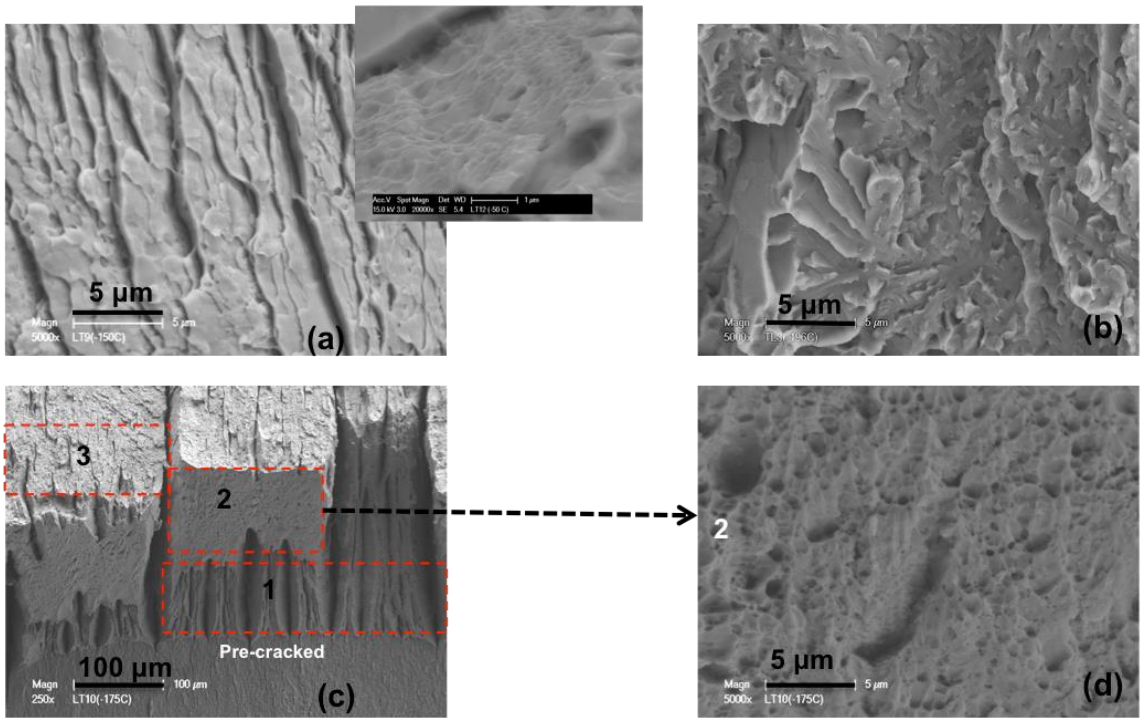
Fig. 8   (a) SEM images of the fracture surfaces showing large shallow dimple-like features at -150ºC and a higher magnification insert showing microvoid dimples on the bottom of the larger features; (b) cleavage facets for the -196°C test, and (c) a L-T fracture surface at -175ºC, revealing delaminations (1), microvoid dimples and craters shown in Fig. d (2), and cleavage facets (3).
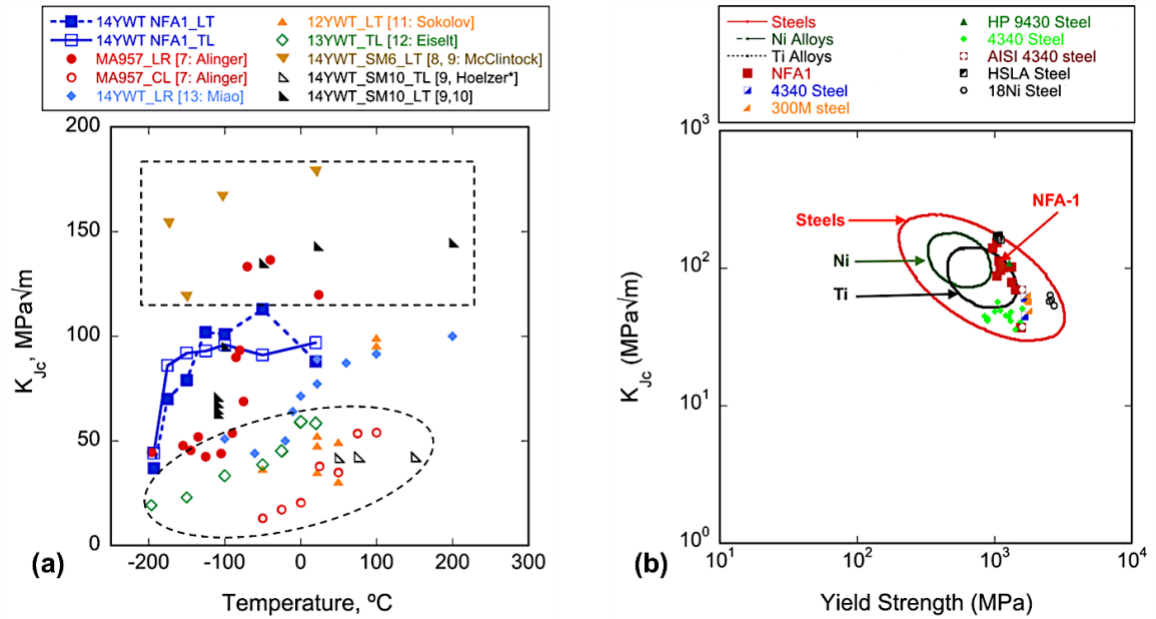
Fig. 9   Comparison of the NFA-1: (a) fracture toughness as a function of temperature with other ODS/NFAs [8-13, Hoelzer: personal communication], and (b) combined strength – K_{Jc} with different alloys [52-56].
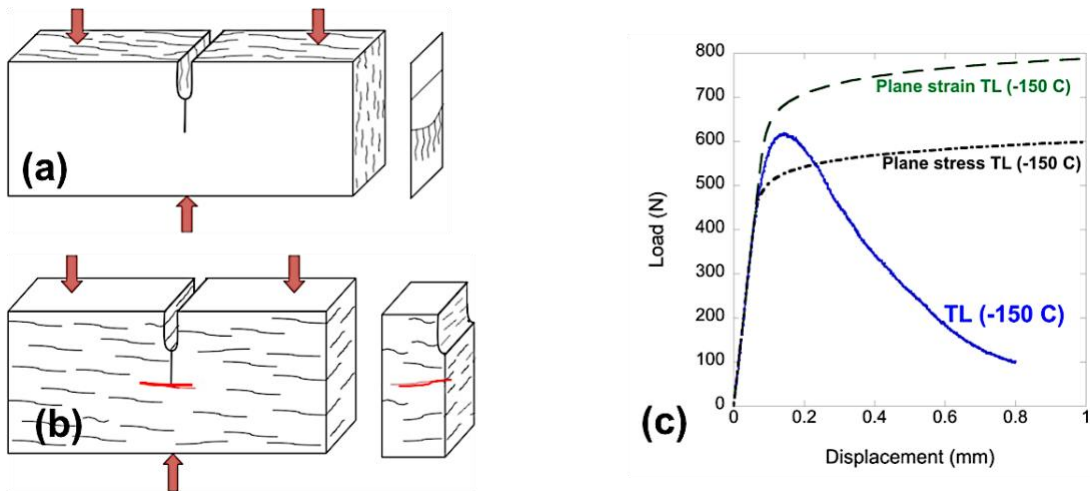

Fig. 10   A schematic illustration of the: (a) transverse delamination mechanism (L-T and T-L); (b) crack deflection mechanism (L-S and T-S); and (c) FEM simulations of load-displacement (P-Δ) for plane strain and stress at -150°C.